

Article

Spatial Oxygen Distribution of the Direct Metal Deposition Process for Different Powder Nozzles

Dominik Keller ^{1,*}, Axel Monney ¹, Timo Schudeleit ²  and Konrad Wegener ¹

¹ Institute of Machine Tools and Manufacturing, ETH Zürich, Leonhardstrasse 21, 8092 Zurich, Switzerland; wegener@iwf.mavt.ethz.ch (K.W.)

² Inspire AG, Technoparkstrasse 1, 8005 Zurich, Switzerland; schudeleit@inspire.ethz.ch

* Correspondence: keller@iwf.mavt.ethz.ch; Tel.: +41-44-633-2178

Abstract: Additive manufacturing processes are among the most innovative manufacturing processes of this century. Powder-based direct metal deposition (DMD) is one of these processes. In the DMD process, local shielding takes place via the powder nozzle. The process is therefore critical for oxidation, especially for materials with an affinity for oxidation such as titanium, aluminum and their alloys. In order to study the oxidation behavior in more detail, the present gas dynamics must be further understood. Wirth and Wegener have made a first approach with their gas flow simulation. In this study, a measurement method for spatial oxygen concentration determination is presented. It can be shown that the spatial oxygen concentration follows the nozzle geometry. Furthermore, the coaxial nozzle is superior to the three-jet nozzle with respect to a low oxygen concentration from a carrier gas to shielding gas volume flow ratio of equal to or greater than 0.4. Finally, it can be shown that the use of a shielding gas chamber eliminates the optimization of the gas flow settings.

Keywords: additive manufacturing; direct metal deposition; CFD simulation; oxygen concentration; powder nozzles



Citation: Keller, D.; Monney, A.; Schudeleit, T.; Wegener, K. Spatial Oxygen Distribution of the Direct Metal Deposition Process for Different Powder Nozzles. *Appl. Sci.* **2023**, *13*, 9470. <https://doi.org/10.3390/app13169470>

Academic Editor: Cem Selcuk

Received: 12 June 2023

Revised: 7 August 2023

Accepted: 18 August 2023

Published: 21 August 2023



Copyright: © 2023 by the authors. Licensee MDPI, Basel, Switzerland. This article is an open access article distributed under the terms and conditions of the Creative Commons Attribution (CC BY) license (<https://creativecommons.org/licenses/by/4.0/>).

1. Introduction and State of Research

Laser cladding is becoming increasingly widely used, especially with today's push for additive manufacturing capabilities as well as life cycle improvements of products. With the increase in applications, the number of newly developed materials for laser cladding has also increased. These new materials also increase the need for a more detailed process understanding to be able to deliver their best performance after being clad. One additive manufacturing technique is powder-blown laser direct metal deposition, which is part of the scope of this publication.

Investigation of process parameters such as laser power, feed rate, mass flow rate and spot diameter for iron- and nickel-based alloys on metallurgical bonding, microstructure, porosity and cracking tendency have been the main focus of research in additive manufacturing technology so far [1–5]. This is sufficient in most cases for the above-mentioned iron- and nickel-based alloys. For materials with an affinity for oxidation, such as titanium or aluminum alloys, consideration of the usual process parameters, which are intended to ensure sufficient energy input for the build-up, is not sufficient. The present gas dynamics have a significant impact on the oxidation. Oxidation leads to unfavorable material properties such as the embrittlement of titanium. In powder-based direct metal deposition (DMD), the melt pool is protected against oxidation by the shield gas flow. In powder-based DMD, the gas dynamics are adjusted by the two machine parameters shielding gas volume flow and carrier gas volume flow. In the following, the state of research is presented which deals with the shielding gas atmosphere of the powder-based DMD process.

Yamaguchi and Hagino [6] investigated the impact of the ambient oxygen concentration in the resulting material deposition quality regarding WC-12Co coatings. In this

investigation, a shielding gas chamber was used, in which a precise ambient oxygen concentration could be set and held during a normal cladding run. Furthermore, the laser power was changed during the experiments to see the impact of the laser power combined with the oxygen concentration. Single tracks were deposited at different laser powers and oxygen concentrations. The cross sections were analyzed using optical microscopy as well as X-ray diffraction (XRD) to obtain an impression of pores and their size as well as the material composition. As main result of this study, the increase in the pore size in the build-up with increasing oxygen concentration is revealed. The main issue of this study is that no element analysis was performed. Thus, no reliable statement can be made whether the pores resulted from the change in oxygen concentration. Furthermore, it is also not possible to explain the contrary behavior that the porosity increase is due to exceeding a certain limit power. One possibility is that the increasing melt pool dynamics at higher temperatures and the decomposition of the hard-phase particles creates additional pores. Whether the porosity is ultimately determined by the oxygen concentration cannot be clearly concluded from this study. Furthermore, the influence of the nozzle geometry and the influence of the carrier gas and shield gas volume flow on the present oxygen concentration is not investigated. This will be investigated in more detail within the scope of the present study.

Koruba et al. [7] have investigated the impact of process gases on Stellite 6 coatings onto a cylindrical steel substrate. The influence of carrier gas and shielding gas variation on the following coating properties were investigated: coating height, depth of the heat affected zone, roughness and microhardness. The study demonstrates that by increasing the carrier gas flow, the roughness of the surface decreases, thus reducing the formation of surface discontinuities. Furthermore, with increasing carrier gas flow, the depth of the heat affected zone, the height of the layer and the dilution increases. With increasing shielding gas flow, coating irregularities increase. On the other hand, the depth of the heat-affected zone decreases with increasing shielding gas flow due to the higher cooling rate caused by the higher shielding gas flow. Due to the higher cooling rate, the microhardness increases. The study clearly illustrates the influence of the process gases on the coating properties. However, only geometrical and mechanical properties are investigated based on the permutation of two gas settings (carrier gas: 4 L/min and 10 L/min and shield gas: 10 L/min and 15 L/min). A reliable statement cannot be made due to the low number of samples investigated. Furthermore, the influence of the gas settings on the gas velocity was investigated by means of a CFD simulation. This does not allow final conclusions to be drawn about the spatial oxygen concentration. An increase in microhardness could also be due to an increase in oxidation. Since no element analysis was carried out, the statement of this paper is not unambiguous. Finally, the influence of the nozzle geometry on the oxygen concentration was not investigated; this will be investigated in the following study in more detail.

Wirth and Wegener [8] performed a simulation and parameter study looking at different gas types (He and Ar) with different three-jet nozzles while characterizing their performance regarding powder particle speed, oxygen concentration and shielding capabilities of both process gases. It was shown that changing the carrier gas species has an effect on the oxygen concentration. Due to its lower molar mass compared to Ar, He has a smaller influence on the protective gas flow at the same carrier gas flow and thus leads to a lower oxygen concentration. Furthermore, it can be seen that the shielding gas bell is increasingly disturbed with an increase in the carrier gas flow. However, the oxygen concentration was only measured exactly below the nozzle, so no spatial oxygen concentration can be drawn experimentally. Furthermore, only two different three-jet nozzles were investigated and no comparison with other nozzle geometries (e.g., a coaxial nozzle) was provided.

The aims and objectives of this study differ from the existing studies in the following points:

- (1) Specification of the gas dynamics and the resulting present oxygen concentration over a larger parameter range;

- (2) Description of the influence of different nozzle geometries (in particular a coaxial nozzle) must be investigated in more detail;
- (3) Simulation of the coaxial nozzle in terms of resulting oxygen concentration depending on different gas flow settings.

2. Experimental Setup and Methods

Two nozzles with different geometries were measured regarding oxygen concentration distribution. These are a three-jet nozzle, which is an in-house product of *Oerlikon Metco* and not commercially available, and the *Coax 40S* coaxial nozzle from *Fraunhofer ILT*. The *Metco* powder nozzle has a powder channel diameter of $d_c = 2$ mm and a standoff of 12 mm. Standoff is defined as the distance between the nozzle tip and the powder focus. The *ILT* coaxial nozzle has an angular cavity of $200\ \mu\text{m}$ between the outer and inner cone and a standoff of 7 mm. The experimental setup (see Figure 1) was developed for the measurement.

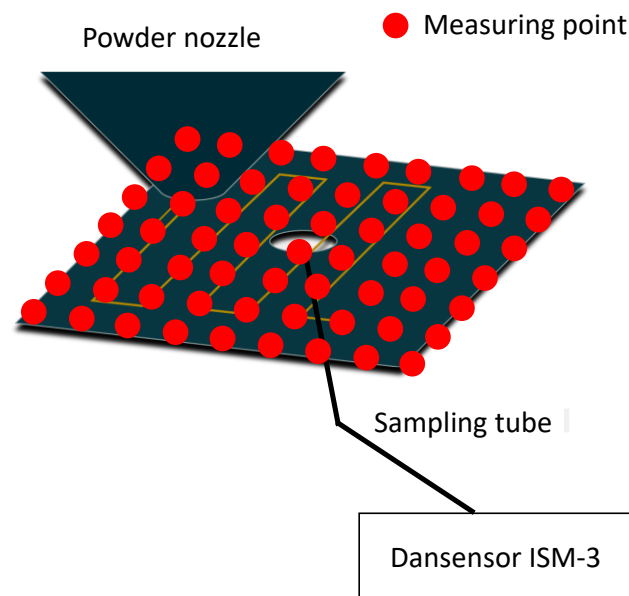


Figure 1. Measuring principle for determining the spatial oxygen concentration. A scanning strategy or a stationary measurement can be utilized.

A hole plate was fabricated so that the diameter of the hole matches the outside diameter (diameter: $1/16''$) of the sampling tube of the oxygen sensor. The *Dansensor ISM-3* was used to measure the oxygen concentration with an accuracy better than $\pm 1\%$ of the displayed measured value.

To obtain a first insight into the spatial extent of the zone with low oxygen concentration ($<10,000$ ppm), both nozzles were approached from the outside in the direction of the gas sampling hose at a carrier gas flow of 4 L/min and a shield gas flow of 15 L/min at the working distance of the respective nozzle (standoff three-jet nozzle: 12 mm, standoff coaxial nozzle: 7 mm) until a change to the ambient oxygen concentration (20.9 vol.%) occurred. Below a certain distance, a strong oxygen gradient was present. To better resolve this area, the point grid was refined in this region.

These experiments were used to create an oxygen concentration distribution at the respective working distance of each nozzle with turned off laser and powder flow. The laser must be turned off because it would destroy the gas sampling hose and the powder flow must be turned off because it would destroy the ceramics which are inside the oxygen sensor. This has no impact on the measured oxygen concentration because the influence of thermally induced flows is negligible (which is shown in the Numerical Modeling section) and because of the low volume percentage of the powder particles inside the carrier gas

flow. Further experiments investigating the oxygen concentration change directly above the gas sampling hose (at working distance of the respective nozzle) at different carrier and shield gas flows were performed. Those allowed us to investigate the change in oxygen concentration depending on the carrier and shield gas flows.

In addition to the nozzle characterization in ambient environment, the oxygen distribution measurements were performed inside a shield gas chamber to measure the impact of the chamber on the resulting oxygen concentration.

Therefore, the oxygen point grid experiments were repeated, as well as the carrier and shield gas variations. The influence of the shield gas chamber on the spatial oxygen concentration can thus be demonstrated.

Before the measurements could be carried out in the shielding gas chamber, the shortcomings of the shielding gas chamber regarding ventilation still had to be eliminated. Due to the lack of pressure equalization holes as well as the one-sided ventilation, a homogeneous inflow in the shielding gas chamber is not possible. This results in too high oxygen concentrations (2231 ppm) inside the chamber, as can be seen on the oxygen sensor display (see Figure 2).

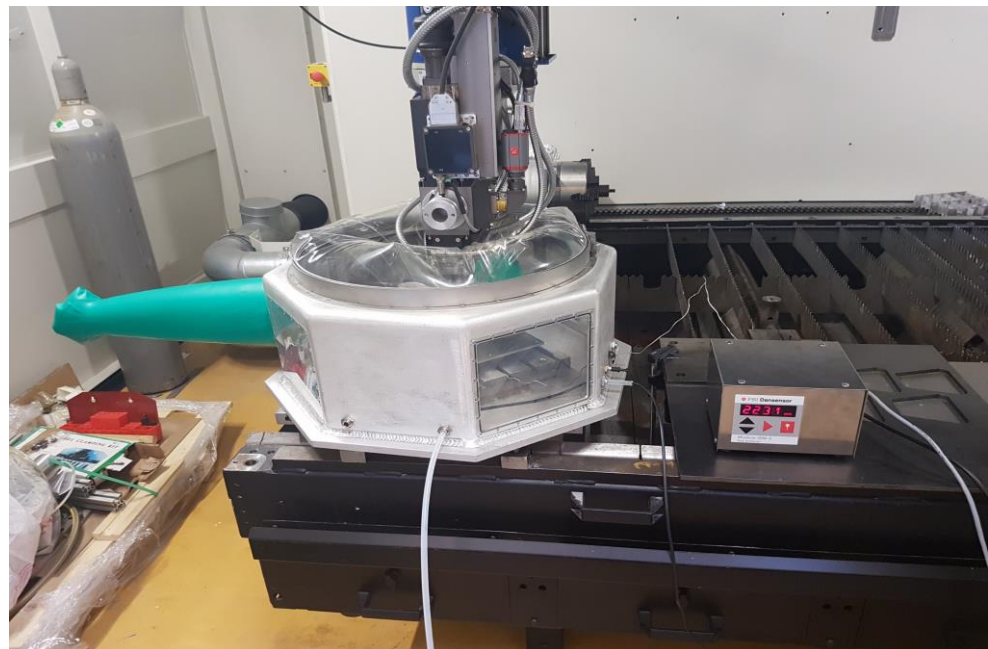


Figure 2. The unfavorable, original ventilation possibility of the shielding gas chamber leads to an inhomogeneous flow profile as well as turbulence within the chamber. This can be seen from the inflated gloves and the high oxygen concentration within the chamber.

To achieve a more homogeneous inflow, pressure equalization holes were fabricated on the top of the chamber and a diffuser ring was 3D printed, which was flow optimized using computational fluid dynamics simulations (see Figure 3).

The diffuser ring with the slit (bottom picture of Figure 3) allows a uniform, homogeneous inflow of argon from all directions at simultaneous low inflow velocities. This avoids turbulence within the shielding gas chamber, which has a favorable effect on the present oxygen concentration. After an influx of Ar for 10 min, the oxygen concentration within the chamber was <150 ppm. After this time, the experiments were started with each nozzle in the chamber.

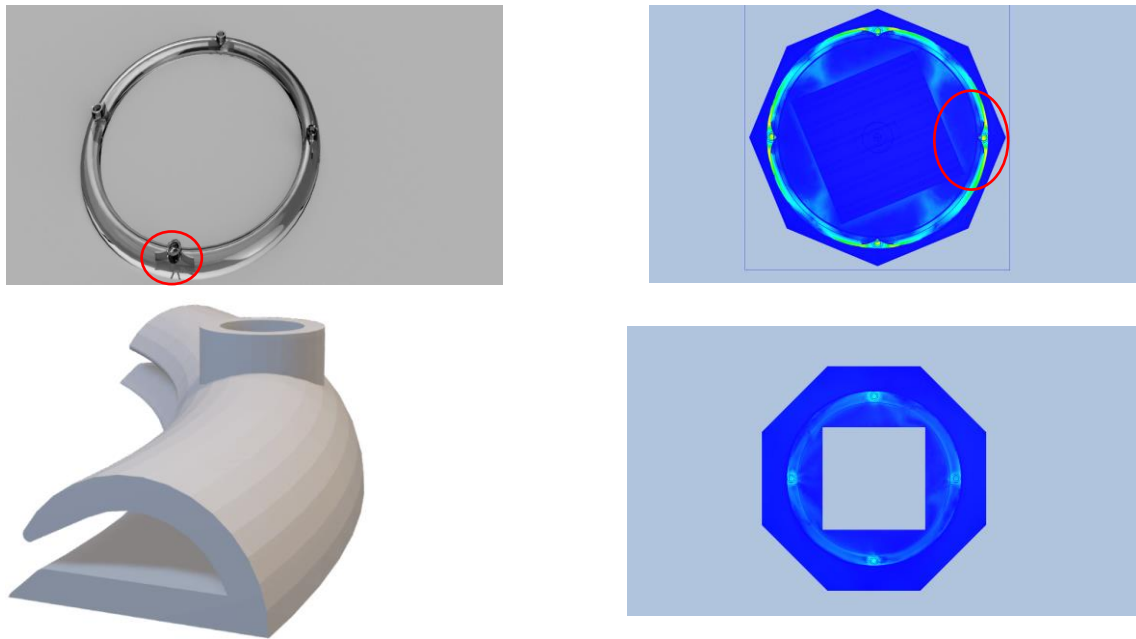


Figure 3. (Top left): Unfavorable inflow conditions due to fin (marked in red). This results in high inflow velocities (top right). (Bottom): Favorable design with slit results in low inflow velocities (bottom right).

2.1. Point Grid Measurements

For the stationary point grid measurement as shown in Figure 1, a measuring grid was used that becomes finer towards the center. The point grid was refined at locations where a high-oxygen gradient occurred. The exact global positions of measuring points are shown in Tables A1 and A2 in the Appendix A. The two nozzles were each positioned at their working distance (WD) above the hole plate. The WD of the three-jet nozzle is 12 mm and it is 7 mm for the coaxial nozzle. The relative coordinate positions of the coaxial and the three-jet nozzle differ due to the different behavior of the two nozzles with respect to the present oxygen concentration. Ar was used as the shielding and carrier gas. The volume flows have been set to $\dot{V}_C = 4 \text{ L/min}$ and $\dot{V}_S = 15 \text{ L/min}$.

The axial measurements served to delimit the area of interesting low oxygen concentration and to spatially specify where the high oxygen gradient is present. In the region of low oxygen concentration, radial measurements were performed. Since there exist symmetries, the 1st and 4th quadrants were measured for the three-jet nozzle, since it is symmetric along the y -axis, as can be seen in Figure 4. Due to the rotational symmetry of the coaxial nozzle, only the 1st quadrant was measured for this nozzle.

2.2. Measurements at Centrum ($x = 0, y = 0$)

To determine the influence of the volume flow ratios of carrier gas to shielding gas, measurements were carried out centrally above the bore of the hole plate at the working distance ($x = 0, y = 0, z = \text{WD}$) of the respective nozzle for the three-jet and the coaxial nozzle. The following volume flow variations were carried out:

- \dot{V}_C : 4 L/min to 12 L/min in steps of 4 L/min;
- \dot{V}_S : 7.5 L/min to 30 L/min in steps of 7.5 L/min.

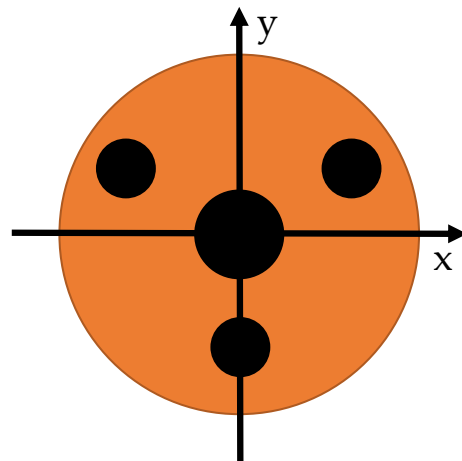


Figure 4. Illustration of the symmetry of the three-jet nozzle along the *y*-axis. For the three-jet nozzle, the 1st and 4th quadrants were measured. For the coaxial nozzle, the measurement of the 1st quadrant is sufficient.

3. Numerical Modeling

The geometry of the three-jet nozzle and the coaxial nozzle were modeled in COMSOL Multiphysics 6.0 as displayed in Figure 5.

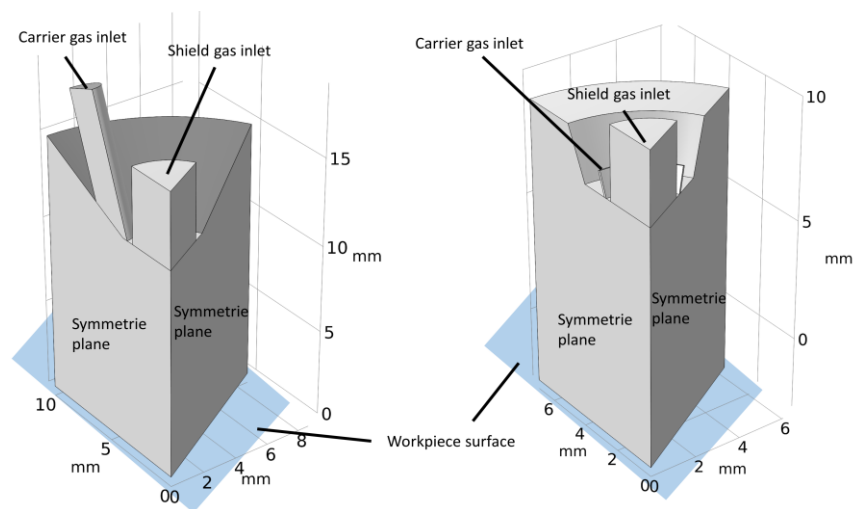


Figure 5. Model domains for the CFD simulation. (Left): Three-jet nozzle. (Right): Coaxial nozzle.

The basic model for the flow simulation is the model of Wirth and Wegener. Due to the symmetry of the problem, one-sixth of each nozzle is simulated. The fluid flow can be described by the continuity equation [9] and the stationary Navier–Stokes equation for incompressible fluids ($Ma < 0.3$ and therefore pressure changes associated with the dynamic pressure can be neglected) [9].

$$\rho \nabla \cdot u = 0 \tag{1}$$

$$\rho(u \cdot \nabla)u = \nabla \cdot \left\{ -p \cdot I + (\mu + \mu_t)[\nabla \otimes u + (\nabla \otimes u)^T] \right\} + F \tag{2}$$

where ρ is the density, u is the velocity vector, p is the pressure, I is the unit tensor, μ is the dynamic viscosity, μ_t is the eddy viscosity according to Wilcox [10] and F is the volume force. The Nabla operator is coupled to the velocity vector via the tensor product (symbol:

⊗). The values for the eddy viscosity and the wall functions as well as their calculation are given by Wirth and Wegener [8].

The oxygen concentration is influenced by the mixing of the various gases involved. The mixing of the gases occurs through diffusion and thermal effects. The model domain contains Ar and air. Air has an oxygen concentration of about 20.9 vol.%. In the following, the different gases are referred to as species.

The mixing due to diffusion can be described by the general mass transport equation [11].

$$\frac{\partial}{\partial t}(\rho\omega_i) + \nabla \cdot (\rho\omega_i u) = -\nabla \cdot j_i + R_i \tag{3}$$

Since this is a stationary problem, the first, the time-dependent term is omitted. Furthermore, there are no chemical reactions of the species involved. Therefore, the term R_i is obsolete. This term is the rate expression describing the production or consumption of species i . This simplifies Equation (3) to:

$$\nabla \cdot (\rho\omega_i u) = -\nabla \cdot j_i \tag{4}$$

Equation (4) considers with the mass flow of species i [11] diffusive transport, convective transport and the turbulent mixing of the mass fraction ω_i of species i . The calculation of the turbulent mixing coefficient D_t , the mean molar mass M as well as the calculation of the mixture-averaged diffusion coefficient D_i^m of species i can be found in Wirth and Wegener [8]. The mixed gas is treated as an ideal gas.

$$j_i = -\rho(D_i^m + D_t)(\nabla\omega_i + \omega_i\nabla M/M) \tag{5}$$

The basic model of Wirth and Wegener considers the mixing due to diffusion, which is considered in Equations (4) and (5).

4. Results and Discussion

4.1. Simulation Results

In order to determine the influence of the nozzle geometry and the carrier gas flow on the present oxygen concentration, a parameter sweep of the carrier gas volume flow and shield gas volume flow were carried out for both nozzles. Results are shown in Figures 6 and 7.

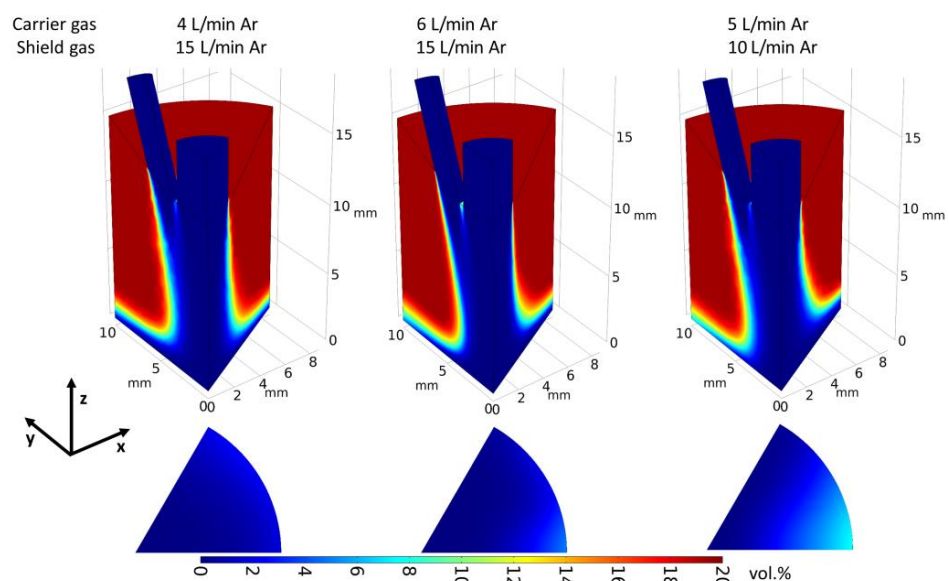


Figure 6. Parametric sweep of the carrier gas volume flow and shield gas volume flow of the three-jet nozzle. **Top:** Oxygen concentration in an isometric view. **Bottom:** Oxygen concentration on workpiece surface.

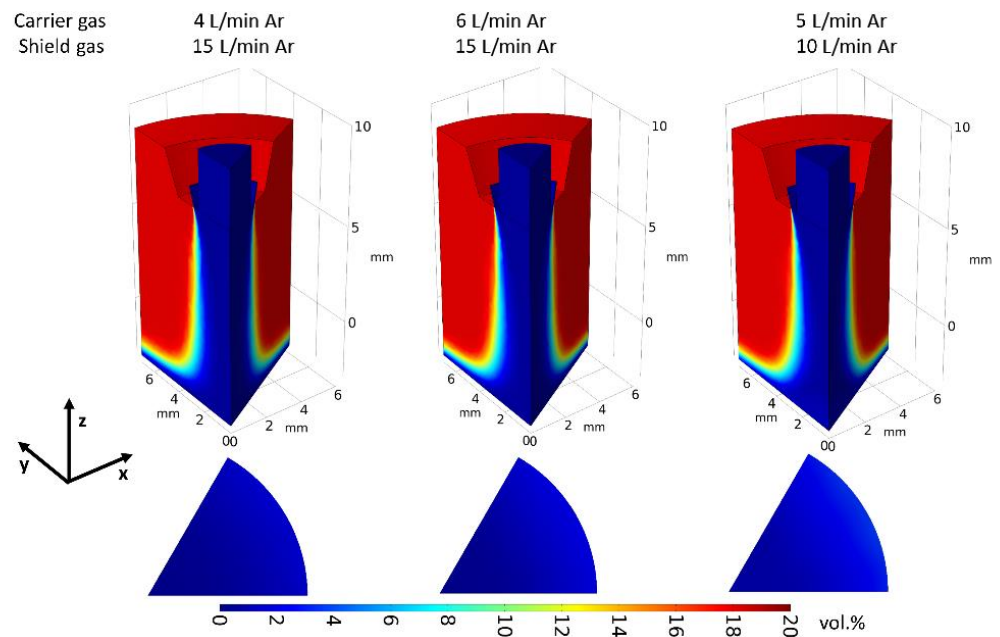


Figure 7. Parametric sweep of the carrier gas volume flow and shield gas volume flow of the coaxial nozzle. **Top:** Oxygen concentration in an isometric view. **Bottom:** Oxygen concentration on workpiece surface.

As can be seen from Figures 6 and 7, the three-jet nozzle is more sensitive to a variation in the carrier and shield gas volume flow in relation to the coaxial nozzle. From a carrier gas flow to shield gas volume flow ratio of greater than 0.4, the three-jet nozzle exhibits significantly higher oxygen concentrations. Furthermore, the oxygen concentration on the substrate surface is more homogeneous for the coaxial nozzle.

4.2. Experimental Results

4.2.1. Experiments without Shield Gas Chamber

The result of the data analysis with Python of the oxygen point grid experiments of the three-jet nozzle are depicted in Figure 8.

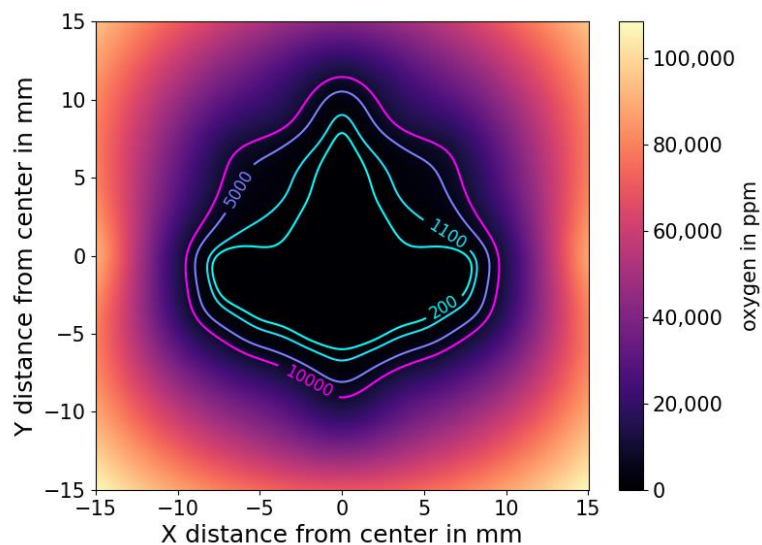


Figure 8. Detailed view of the center with low oxygen concentrations for the three-jet nozzle.

Figure 8 shows a pronounced three-jet symmetry of the oxygen concentration distribution, which results from the nozzle geometry. The openings of the powder channels of

the three-jet nozzle are located at the extended points of the contour lines. The symmetry results in a directional dependence of the three-jet nozzle in relation to the spatially present oxygen concentration distribution.

The result of the data analysis of the oxygen point grid experiments of the coaxial nozzle are shown in Figure 9.

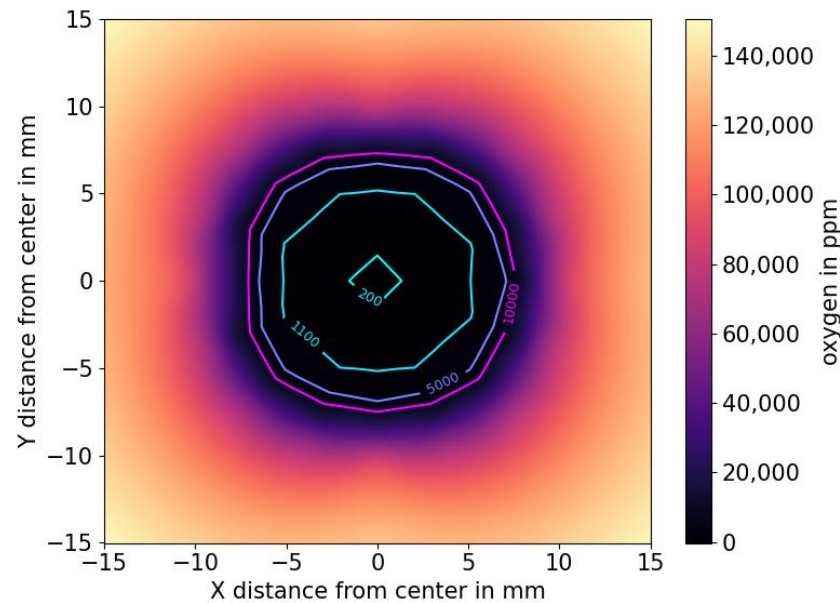


Figure 9. Spatial oxygen distribution of the coaxial nozzle.

Figure 9 shows a sharp, defined center of low oxygen concentrations. Over a range of approximately a 7 mm radius, an oxygen concentration smaller than 10,000 parts per million (ppm) oxygen can be achieved. Furthermore, there is no directional dependence of the coaxial nozzle. In general, in contrast to the three-jet nozzle, a more homogeneous picture of low oxygen concentration is obtained. Since the carrier gas flow is spatially introduced equally from all the spatial directions, a radial symmetry of the oxygen concentration distribution results. Therefore, the carrier gas flow has less influence on the shield gas flow, resulting in less turbulence disturbing the shield gas cap.

The influence of the volume flows is shown subsequently. Figure 10 shows the influence of the carrier gas flow on the existing oxygen concentration at the working distance of the respective nozzle centered above the hole plate.

The carrier gas flow has an influence on the existing oxygen concentration. The standard deviation of the measuring points was determined based on three measurements. It is not visible in the diagram because the standard deviation for all measurements is less than 200 ppm and thus smaller than the marking of the points in the diagram. Thus, a statistical significance of the carrier gas volume flow on the oxygen concentration is given. Furthermore, the coaxial nozzle is less sensitive to carrier gas flow variation. In general, it can be stated that the oxygen concentration increases with increasing carrier gas volume flow (see trend line in Figure 10), and the coaxial nozzle is more robust to an increase in carrier gas volume flow in comparison to the three-jet nozzle.

Figure 11 shows the influence of the shield gas flow on the existing oxygen concentration at the working distance of the respective nozzle centered above the hole plate.

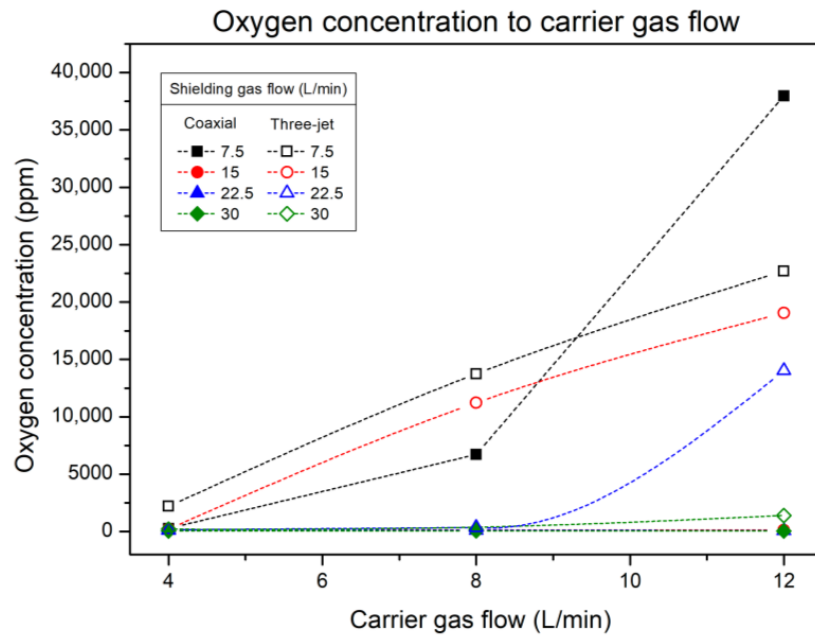


Figure 10. Influence of the carrier gas flow on the present oxygen concentration. Measurements were carried out directly above the hole plate in the working distance of the respective nozzle.

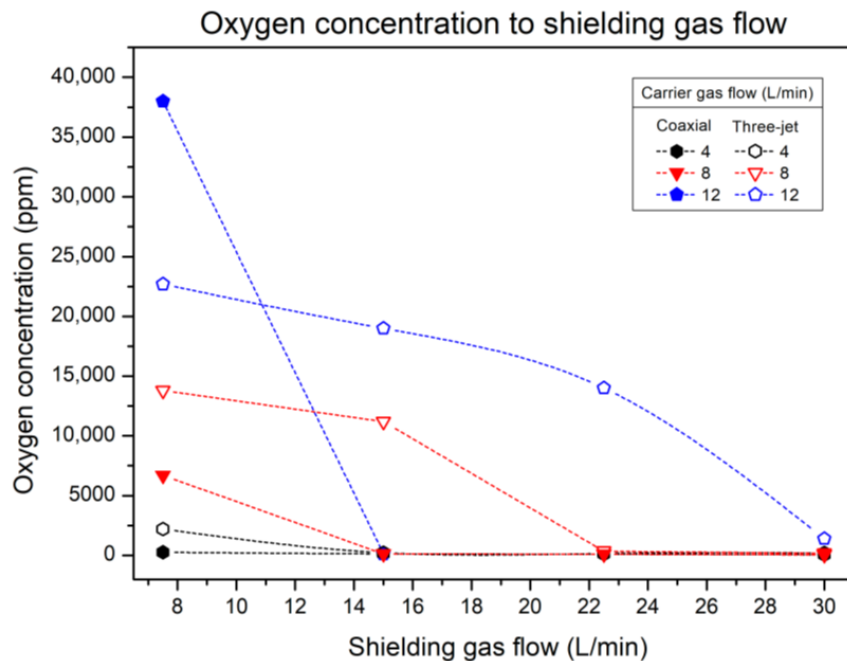


Figure 11. Influence of the shield gas flow on the present oxygen concentration. Measurements were carried out directly above the hole plate in the working distance of the respective nozzle.

As the shield gas flow increases, the oxygen concentration decreases. The spread of the oxygen concentrations (e.g., at a shield gas flow of 7.5 L/min) results from the fact that a higher carrier gas volume flow was used at the higher oxygen concentrations—in contrast, lower carrier gas volume flows were used at lower oxygen concentrations at a shield gas flow of 7.5 L/min. It can also be seen that the coaxial nozzle tends to have lower oxygen concentrations with the same shield gas flow. Looking at the gradients of the trend lines, the carrier gas volume flow has a greater influence on the oxygen concentration present than the shield gas flow. This proves that a suitable adjustment of the carrier gas volume flow has a significant influence on the spatial oxygen distribution on the melt pool surface.

To clarify whether the present oxygen concentration can be described by the ratio of carrier gas volume flow to shield gas volume flow, the oxygen concentration was plotted versus this ratio in Figure 12.

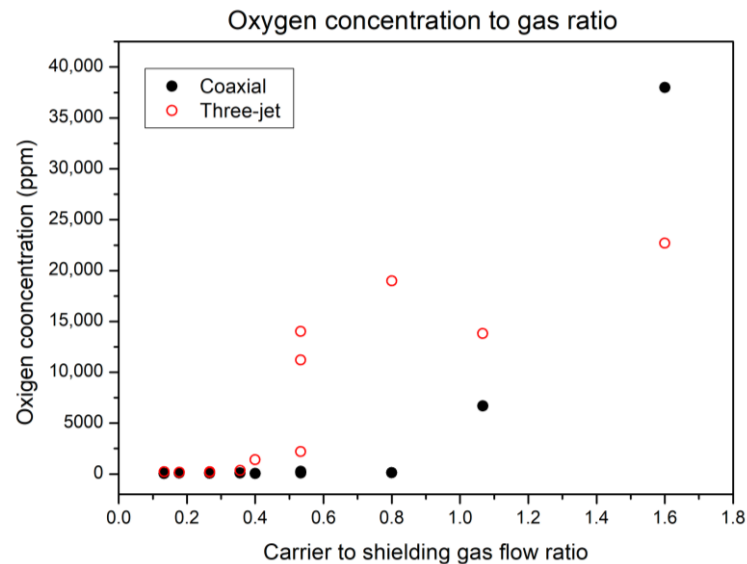


Figure 12. Influence of the carrier gas flow to shield gas flow ratio on the present oxygen concentration.

Figure 12 illustrates the robustness of the coaxial nozzle to an increasing carrier gas flow to shield gas volume flow ratio. For a ratio of the carrier gas volume flow to shield gas volume flow of less than 0.4, the oxygen values of the two nozzles are in a similar range. From this ratio, the three-jet nozzle has a significantly higher oxygen concentration compared to the coaxial nozzle. Only for the highest ratio (1.6) does the coaxial nozzle perform worse. But in practice, this ratio is of no relevance, because such a high carrier gas flow is not used due to the high argon consumption and the induced turbulence in the shielding gas bell. Furthermore, it can be seen that the three-jet nozzle at a gas ratio of 0.53 performs worse with higher shielding gas flows (15 L/min and 22.5 L/min) with regard to a low oxygen concentration. This anomaly can be explained by the Venturi effect. Due to the higher flow rate of the shielding gas fluid, the static pressure of the fluid is lower than the pressure of the ambient air. This negative pressure allows oxygen to be sucked into the shielding gas bell from the ambient air.

Summing up, Figures 8 and 9 show that the present spatial oxygen concentration follows the nozzle geometry and is more sharply limited for the coaxial nozzle. Figure 10 illustrates the oxygen increase under the nozzle with increasing carrier gas flow; this is more noticeable for the three-jet nozzle. This demonstrates the greater robustness of the coaxial nozzle to carrier gas volume flow variations. Figure 11 shows the decrease in oxygen concentration with increasing shielding gas flow. Figure 12 shows that from a carrier gas volume flow to shielding gas volume ratio of equal to/greater than 0.4, the coaxial nozzle performs significantly worse with respect to present oxygen concentration. It can thus be concluded that for oxidation-critical materials such as titanium and aluminum, the coaxial nozzle has significant advantages over a three-jet nozzle regarding oxidation.

4.2.2. Experiments with Shield Gas Chamber

Figure 13 shows the influence of the carrier gas volume flow to shielding gas volume flow ratio on the oxygen concentration of the three-jet nozzle and the coaxial nozzle inside the shield gas chamber.

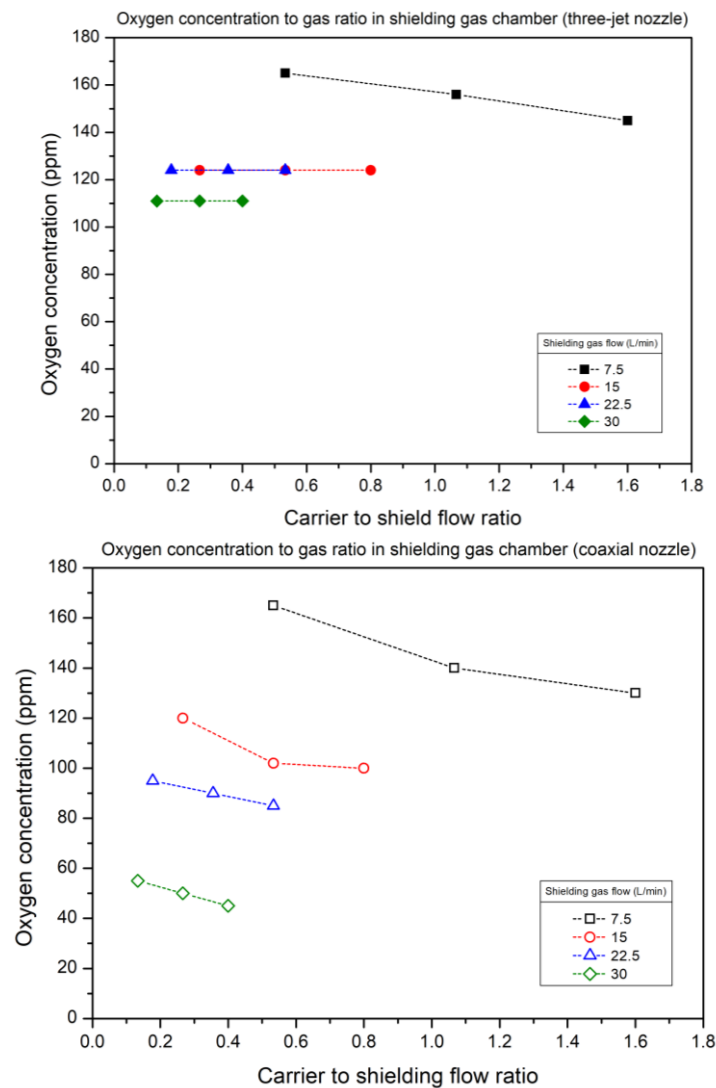


Figure 13. Influence of the shield gas chamber on the oxygen concentration for various carrier to shield gas flow ratios. **Top:** Three-jet nozzle. **Bottom:** Coaxial nozzle.

Figure 13 shows that the shielding gas chamber practically eliminates the influence of the carrier gas volume flow to shield gas volume flow ratio for both nozzles. Even for the very large ratio of 6, no significant increase in oxygen concentration is found for the three-jet nozzle. There is a tendency of improvement in oxygen concentration at the same gas ratio with increasing shielding gas volume flow for both nozzles. Furthermore, the coaxial nozzle exhibits a lower oxygen concentration at the same gas ratio for shielding gas volume flows larger than 15 L/min.

5. Conclusions and Future Work

The present study describes an experimental procedure for determining the spatial oxygen concentration of the direct metal deposition process. Furthermore, the influence of the carrier gas volume flow on the shield gas volume flow is presented. Furthermore, a numerical model is developed that considers thermal effects on the resulting oxygen concentration. The results confirm that the nozzle type and gas settings have a noteworthy influence on the oxygen concentration. This can be used to improve the quality of AM parts made from oxidation-critical materials. The experimental results and the simulation led to the following conclusions:

- The simulation of the oxygen concentration is congruent with the results of the experimental oxygen measurements.

- The spatial oxygen concentration of the three-jet nozzle is less pronounced in comparison to the coaxial nozzle. The center of low oxygen concentration follows the nozzle geometry.
- The carrier gas volume flow has a greater impact on the oxygen concentration compared to the shield gas volume flow.
- The coaxial nozzle is less sensitive to gas ratio variations than the three-jet nozzle. From a carrier gas volume flow to shield gas volume flow ratio of 0.4, the three-jet nozzle leads to high oxygen concentrations.
- A shield gas chamber practically eliminates the influence of the gas settings on the present oxygen concentration.

In further studies, it is necessary to clarify which oxygen concentration in AM parts with oxidation-critical materials can be achieved with the present nozzle types with and without a shield gas chamber at different gas settings. In the case of Ti_6Al_4V , the microstructure must not contain an oxygen concentration greater than 2000 ppm. Furthermore, an oxidation model should be developed that can be used to estimate whether the process is oxidation-critical or not.

Author Contributions: Conceptualization, D.K. and K.W.; methodology, D.K. and A.M.; software, D.K. and A.M.; validation, D.K., A.M., T.S. and K.W.; investigation, D.K. and A.M.; resources, K.W.; writing—original draft preparation, D.K.; writing—review and editing, A.M., T.S. and K.W.; visualization, D.K.; supervision, T.S. and K.W.; project administration, D.K. and K.W.; funding acquisition, K.W. All authors have read and agreed to the published version of the manuscript.

Funding: This research received no external funding.

Institutional Review Board Statement: Not applicable.

Informed Consent Statement: Not applicable.

Data Availability Statement: The datasets generated during and/or analyzed during the current study are available from the corresponding authors on reasonable request.

Conflicts of Interest: The authors declare no conflict of interest.

Appendix A

Table A1. Relative coordinates in mm of the oxygen point grid measurements of the three-jet nozzle. The center of the coordinate system ($x = 0, y = 0, z = 0$) is in the hole of the hole plate.

x	y	z
30	0	WD
25	0	WD
20	0	WD
15	0	WD
10	0	WD
5	0	WD
7.5	0	WD
8	0	WD
7	0	WD
6	0	WD
6.5	0	WD
5.5	0	WD
4.5	0	WD
4	0	WD
3.5	0	WD
3	0	WD
2	0	WD
1	0	WD

Table A1. *Cont.*

x	y	z
0	0	WD
-1	0	WD
-2	0	WD
-3	0	WD
-3.5	0	WD
-4	0	WD
-4.5	0	WD
-5	0	WD
-5.5	0	WD
-6	0	WD
-6.5	0	WD
-7	0	WD
-8	0	WD
-10	0	WD
-15	0	WD
-25	0	WD
-30	0	WD
0	30	WD
0	25	WD
0	20	WD
0	15	WD
0	10	WD
0	9.5	WD
0	9	WD
0	8.5	WD
0	8	WD
0	7.5	WD
0	7	WD
0	6.5	WD
0	6	WD
0	5.5	WD
0	5	WD
0	4	WD
0	3	WD
0	2	WD
0	1	WD
0	0	WD
0	-5	WD
0	-5.5	WD
0	-6	WD
0	-6.5	WD
0	-7	WD
0	-7.5	WD
0	-8	WD
0	-8.5	WD
0	-9	WD
0	-9.5	WD
0	-10	WD
0	-11	WD
0	-15	WD
0	-20	WD
0	-25	WD
0	-30	WD

Table A2. Relative coordinates in mm of the oxygen point grid measurements of the coaxial nozzle. The center of the coordinate system ($x = 0, y = 0, z = 0$) is located in the hole of the hole plate.

x	y	z
30	0	WD
25	0	WD
20	0	WD
15	0	WD
10	0	WD
5	0	WD
7.5	0	WD
8	0	WD
8.5	0	WD
7	0	WD
6.5	0	WD
6	0	WD
5.5	0	WD
4	0	WD
3	0	WD
2	0	WD
1	0	WD
0	0	WD
-1	0	WD
-2	0	WD
-3	0	WD
-4	0	WD
-5	0	WD
-5.5	0	WD
-6	0	WD
-6.5	0	WD
-7	0	WD
-7.5	0	WD
-8	0	WD
-8.5	0	WD
-10	0	WD
-15	0	WD
-20	0	WD
-25	0	WD
-30	0	WD
0	30	WD
0	25	WD
0	20	WD
0	15	WD
0	10	WD
0	8.5	WD
0	8	WD
0	7.5	WD
0	7	WD
0	6.5	WD
0	6	WD
0	5.5	WD
0	5	WD
0	4	WD
0	3	WD
0	2	WD
0	1	WD
0	-1	WD
0	-2	WD
0	-3	WD
0	-4	WD
0	-7	WD
0	-5	WD

Table A2. Cont.

<i>x</i>	<i>y</i>	<i>z</i>
0	−5.5	WD
0	−6	WD
0	−6.5	WD
0	−7	WD
0	−7.5	WD
0	−8	WD
0	−8.5	WD
0	−10	WD
0	−15	WD
0	−20	WD
0	−25	WD
0	−30	WD

References

- Herzog, D.; Seyda, V.; Wycisk, E.; Emmelmann, C. Additive manufacturing of metals. *Acta Mater.* **2016**, *117*, 371–392. [[CrossRef](#)]
- Oliveira, J.P.; LaLonde, A.D.; Ma, J. Processing parameters in laser powder bed fusion metal additive manufacturing. *Mater. Des.* **2020**, *193*, 108762. [[CrossRef](#)]
- DebRoy, T.; Wei, H.L.; Zuback, J.S.; Mukherjee, T.; Elmer, J.W.; Milewski, J.O.; Beese, A.M.; Wilson-Heid, A.; De, A.; Zhang, W. Additive manufacturing of metallic components—process, structure and properties. *Prog. Mater. Sci.* **2018**, *92*, 112–224. [[CrossRef](#)]
- Shamsaei, N.; Yadollahi, A.; Bian, L.; Thompson, S.M. An overview of Direct Laser Deposition for additive manufacturing; Part II: Mechanical behavior, process parameter optimization and control. *Addit. Manuf.* **2015**, *8*, 12–35. [[CrossRef](#)]
- Fayazfar, H.; Salarian, M.; Rogalsky, A.; Sarker, D.; Russo, P.; Paserin, V.; Toyserkani, E. A critical review of powder-based additive manufacturing of ferrous alloys: Process parameters, microstructure and mechanical properties. *Mater. Des.* **2018**, *144*, 98–128. [[CrossRef](#)]
- Yamaguchi, T.; Hagino, H. Effects of the ambient oxygen concentration on WC-12Co cermet coatings fabricated by laser cladding. *Opt. Laser Technol.* **2021**, *139*, 106922. [[CrossRef](#)]
- Koruba, P.; Wall, K.; Reiner, J. Influence of processing gases in laser cladding based on simulation analysis and experimental tests. *Procedia CIRP* **2018**, *74*, 719–723. [[CrossRef](#)]
- Wirth, F.; Wegener, K. Simulation of the multi-component process gas flow for the explanation of oxidation during laser cladding. *Addit. Manuf.* **2018**, *24*, 249–256. [[CrossRef](#)]
- COMSOL Multiphysics 6.1; The Fluid Flow Interface; Reference Manual; COMSOL: Los Angeles, CA, USA, 2023.
- Wilcox, D.C. *Turbulence Modeling for CFD*; DCW Industries: La Canada, CA, USA, 1998; Volume 2, pp. 103–217.
- COMSOL Multiphysics®v. 6.1; Chemical Reaction Engineering Module User’s Guide; COMSOL: Stockholm, Sweden, 2023.

Disclaimer/Publisher’s Note: The statements, opinions and data contained in all publications are solely those of the individual author(s) and contributor(s) and not of MDPI and/or the editor(s). MDPI and/or the editor(s) disclaim responsibility for any injury to people or property resulting from any ideas, methods, instructions or products referred to in the content.